Boundary condition effect on the evaluation of stress triaxiality fields

Andrija Zaplatić, Ana Vrgoč, Zvonimir Tomičević, François Hild

Boundary Condition Effect on the Evaluation of Stress Triaxiality Fields

Andrija Zaplatić[a,b], Ana Vrgoč[a,b], Zvonimir Tomičević[a,*], François Hild[b]

[a] *University of Zagreb, Faculty of Mechanical Engineering and Naval Architecture*
10002 Zagreb, Croatia
[b] *Université Paris-Saclay, CentraleSupélec, ENS Paris-Saclay, CNRS*
LMPS - Laboratoire de Mécanique Paris-Saclay, 91190 Gif-sur-Yvette, France

Abstract

A general framework is presented for evaluating stress triaxiality fields using five different configurations of Dirichlet boundary conditions. The latter ones were measured via stereocorrelation for a simple shear test on a thin sample where buckling was mitigated with an anti-buckling fixture. Friction and material parameters displayed negligible influence on the stress triaxiality fields. Accounting for the anti-buckling fixtures provided the most realistic stress triaxiality fields, but was computationally demanding. Prescribing all out-of-plane displacements, noisier but trustworthy stress triaxiality fields were also obtained by using much less computational resources.

Keywords: Buckling, Dirichlet boundary conditions, inverse problem, simple shear, stereocorrelation

1. Introduction

Thin sheets subjected to metal forming experience elastic springback after their deformation stages. Therefore, it is important to accurately predict reversible

*Corresponding author
Email address: zvonimir.tomicevic@fsb.hr (Zvonimir Tomičević)

deformations. Nowadays, the validity of forming processes is often controlled via Finite Element (FE) analyses that depend on how trustworthy material properties are. Furthermore, product optimization procedures are also governed numerically via FE approaches, thereby improving product design and subsequent manufacturing stages to reduce material waste [1]. Experimental investigations need to be carried out to determine the material response under simple or complex loading regimes. For metal forming, shear is an especially important stress state [2, 3, 4]. However, pure shear stress states cannot be easily achieved experimentally for sheets. As a result, mechanical tests considering simple shear are carried out on thin sheets instead.

Material characterization during mechanical tests where complex loading regimes are employed call for advanced measurement methods. The development of digital imaging provided an opportunity for the emergence of full-field measurement techniques. Digital Image Correlation (DIC) [5, 6, 7, 8, 9, 10] stands out as the most widely employed full-field measurement method due to its versatility and straightforward use. Moreover, the development of global DIC [11, 12, 13, 14] formulated within an FE framework resulted in simple and seamless couplings between experiments and FE simulations. Robust identification methods were designed to utilize this opportunity for the calibration of material parameters.

The resulting output of global DIC is nodal displacements from which strains are calculated. Although displacement and strain fields are readily available with DIC, stress fields cannot be directly measured. The stress fields may be used to evaluate stress triaxiality fields (written as the ratio between hydrostatic and von Mises equivalent stresses). Stress triaxiality plays an important role in damage and

fracture mechanics for predicting the type of failure (*i.e.*, ductile or brittle [15, 16, 17, 18, 19]). Combinations of DIC and X-ray diffraction (XRD) techniques may be used to measure both total and elastic strain fields [20, 21, 22, 23, 23]. The drawback is the required and expensive equipment, as well as the fact that the number of measurement points for XRD is generally limited, and as such, this method is not suited for industrial purposes.

The focus may then shift to analytical and numerical routes instead of experimental investigations to evaluate stress fields. In recent years, several approaches were proposed to assess stress and stress triaxiality fields from DIC measurements. Réthoré [24] developed the so-called Mechanical Image Correlation (MIC) method for evaluating stress fields without assuming any constitutive law. A similar approach where no constitutive laws were defined was used by Dalémat *et al.* [25] where DIC was coupled with a Data Driven Identification algorithm (DDI) for evaluating stress fields. Musiał *et al.* [26] presented an original proposition for evaluating stress fields from DIC data for uniaxial and simple shear tests by considering the measured displacement field gradient and a J_2-plasticity model. The DIC based stress fields gave more accurate results with respect to FE analyses since they accounted for all inaccuracies during experiments. Andrade *et al.* [27] proposed a method to estimate the stress triaxiality fields from DIC strain fields for Von Mises' and Hill's models. Furthermore, Brosius *et al.* [28] developed a similar semi-analytical approach where the stress fields were determined from DIC data. Lindner *et al.* [29] used Integrated DIC to evaluate stress triaxiality fields of a notched titanium alloy sample. It was concluded that even for thin samples, 3D meshes were required to analyze stress triaxiality fields. A similar 3D FE approach was used herein.

Abushawashi *et al.* [30] developed a novel method for constitutive modeling in plane strain conditions. Using DIC data, the authors determined equivalent stress and strain fields to run numerical simulations. From the numerical results, the stress triaxiality fields were evaluated since they display great influence on metal ductility [31, 32, 33]. Brünig *et al.* [34] also combined DIC data with numerical simulations to analyze a biaxial experiment on an H-specimen [35, 36, 37] covering a wide range of stress triaxialities and Lode parameters. Huang *et al.* [38] combined DIC results with computations to evaluate plastic strain and failure of Ti-6Al-4V alloys for specimens with different initial stress triaxialities. Wang *et al.* [39] coupled DIC data with FE runs to study Split Hopkinson Pressure Bar experiments. It was shown that the failure strain decreased with increasing stress triaxiality or strain rate. Peng *et al.* [40] coupled DIC with FE analyses to characterize the stress state of flat metal specimen with inclined notches to analyze the influence of stress triaxiality and Lode angle on failure modes. Pham *et al.* [41] developed a four-node quadrilateral plate element to analyze flexural and buckling responses of a functionally graded plate under different boundary conditions.

Advanced FE-DIC enables for straightforward couplings of measured data with numerical simulations in inverse problems aiming for material parameter calibration [42, 43, 44]. Finite Element Model Updating (FEMU) [45, 46, 47, 48] stands out as the most widely used algorithm for such purposes. With FEMU, the calculated displacement fields and resultant forces are compared to the measured quantities to determine the sensitivity matrices, *i.e.*, how the change in parameters affects them [49, 50, 51]. FEMU was employed for simple (*e.g.*, uniaxial [52]) and more complex (*e.g.*, biaxial [53]) mechanical tests. For identification purposes, the measured displacements were prescribed as Dirichlet boundary conditions on

the FE model. For thin samples, where plane stress states are expected, 2D DIC measurements may be sufficient. However, this approach may be limited when 3D effects cannot be neglected. Réthoré *et al.* [54] proposed a framework where the 3D displacement fields measured with stereocorrelation were used in an integrated procedure. Wang *et al.* [55] also coupled measured 3D displacements with FEMU to describe plastic anisotropy in the so-called Erichsen bulge test.

From the reviewed literature, it is concluded that very few studies combined DIC and FE simulations to assess stress triaxiality *fields* [56, 36, 57, 58]. One key question when coupling experimental and numerical tools is related to boundary conditions. Driving numerical simulations using DIC data for assessing stress triaxiality fields is the goal of this work. To be consistent with the experiment, measured displacements are utilized to drive FE analyses. For that purpose, a monotonic simple shear test was carried out with a Modified Arcan Fixture (MAF) on a 1 mm butterfly shaped specimen, which promoted uniform stress states in the gauge area, made of C60 steel. To measure the surface kinematics, a stereovision setup was used to capture both in-plane and out-of-plane components. Since thin samples subjected to simple shear loading are susceptible to buckling [59], additional supports made of transparent Poly methyl methacrylate (PMMA) were utilized to prevent sample buckling [60, 61, 59, 62]. The experimental setup analyzed herein was developed by Zaplatić *et al.* [63] where thin butterfly samples were subjected to simple shear. The friction coefficient between the PMMA plates and the sample was calibrated numerically via FEMU. To study the effect of prescribed boundary conditions, five test cases were defined, which differed in the definition of the applied kinematics. For each test case, FEMU was carried out to determine the influence of boundary conditions on the calibrated material pa-

rameters. In-depth analyses of the corresponding stress triaxiality fields were conducted for each test case. Such experimental and numerical framework provides a unique approach for analyzing the influence of the prescribed Dirichlet boundary conditions on stress triaxiality fields since the FE simulations were directly driven by experimentally measured DIC data.

2. Experimental protocol

In this section, the entire experimental protocol involving the Modified Arcan Fixture and stereovision system are presented. The stereocorrelation results are then analyzed and discussed.

The experiment presented herein was aimed at preventing buckling of thin sheet samples under simple shear loading. The mechanical test was carried out on a Modified Arcan Fixture (Figure 1), which enables for three loading regimes, namely, shear, tensile and combinations thereof. The MAF employs butterfly shaped samples with two V notches in the middle of the gauge section to promote uniform strain distributions. The expected triaxiality levels in the gauge area (*i.e.*, between the V notches) for the aforementioned loading regimes are 0, 0.33 and 0.66, respectively [63]. The 1-mm thick butterfly sample made of high carbon C60 steel was subjected to simple shear (Figure 1). The experiment was performed on a uniaxial testing machine *Messphysik Beta* 50-5 in displacement control mode with a stroke rate of 1 mm/min. The standard force uncertainty γ_F of the load cell was equal to 10 N.

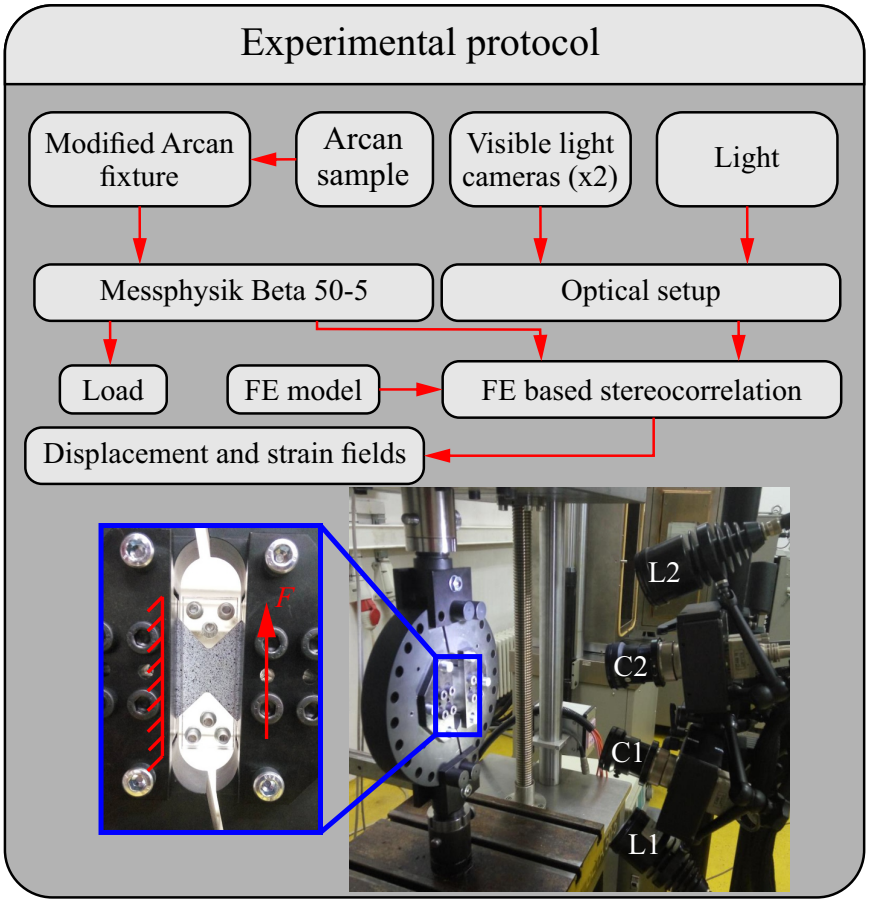

Fig. 1: Experimental workflow with the experimental and optical setup consisting of two vertically positioned visible light cameras (C1 and C2) and two light sources (L1 and L2). On the extracted detail, the Region Of Interest (for stereocorrelation purposes) is depicted on the butterfly sample with the positioned PMMA plates.

Since a thin sample was subjected to simple shear, buckling was expected to occur. In order to mitigate shear buckling, an anti-buckling fixture was designed, which was composed of two 10-mm thick (PMMA) plates. The use of PMMA for the material of the anti-buckling fixture was due to its transparency thus allowing optical measurement methods to be used. Similar setups were employed to minimize buckling and wrinkling of sub-millimeter thick sheets [60, 61, 59]. The

dimensions of the two PMMA plates (*i.e.*, 70×25 mm) were defined with respect to the observable area of the butterfly sample (Figure 1). The plates around both lateral surfaces were connected with a total of six M5 bolts, which were not tightened to reduce the influence of the anti-buckling fixture on the stress triaxiality fields. The material response in the Region Of Interest (ROI) was captured with the stereovision system detailed in Table 1. A total of 900 images was acquired by each camera, where the first ten image pairs corresponded to the unloaded state.

Table 1: Hardware parameters of the stereo-system

Cameras	Dalsa Falcon 4M60
Definition	2358×1728 pixels (B/W images)
Color filter	none
Gray Levels rendering	8 bits
Lens	Titanar 50 mm
Aperture	f/2.8
Field of view	3,996 mm^2
Image scale	≈ 32 pixel/mm
Stereo-angle	25°
Stand-off distance	31.6 cm
Image acquisition rate	1 fps
Patterning technique	B/W paints
Pattern feature size	15 px

The displacement and strain fields of the ROI were measured via FE-based stereocorrelation [64, 65, 66]. The employed software (EikoTwin DIC) consid-

ers a continuous description of the ROI discretized with triangular T3 finite elements [67]. The aforementioned algorithm uses the known geometry of the sample and setup, as observed from the reference images, for calibration purposes. Following the calibration step, shape corrections of the chosen ROI were performed by running a second series of spatial registrations in which out-of-plane corrections were allowed [65]. The stereocorrelation analysis parameters are reported in Table 2. The listed noise floor estimates were determined by calculating the mean temporal standard deviations of each nodal displacement and element strains from the registration of the ten reference image pairs.

Table 2: Stereocorrelation analysis parameters

DIC software	EikoTwin DIC
Image filtering	none
Element length	1 mm
Shape functions	linear (T3 elements)
Mesh	see Figure 3
Matching criterion	penalized sum of squared differences
Regularization length	5 mm
Displacement noise floor (x z y)	0.2 µm 0.1 µm 0.6 µm
Strain ε_{12} noise floor	7×10^{-5}

The global stress/strain response of the sample is shown in Figure 2. The engineering shear stress was calculated by dividing the measured force by the initial cross-sectional area S_0 between the V notches (*i.e.*, 21×1 mm). The strain levels were evaluated by averaging the measured strains within the virtual gauge located

between the V notches of the DIC mesh (Figure 3(c)). The yield stress was approximately equal to 248 MPa (for an offset strain of 0.4%). For the highest load level (*i.e.*, 8.7 kN), the ultimate shear strength was equal to 417 MPa, and the corresponding shear strain 48.7%. From the deformed sample, two distinct symmetric cracks were observed (Figure 2). The initial location of the cracks correlated with tensile stress areas (*i.e.*, with expected stress triaxiality of 0.33). Slight buckling of the central region was also distinguished, especially where compressive stress states were expected (depicted by green rectangles in Figure 2).

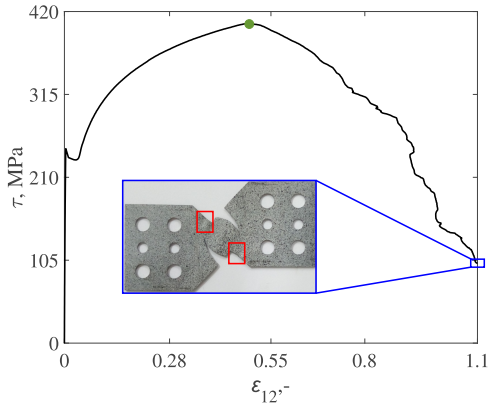

Fig. 2: Macroscopic shear stress/strain response. The green point indicates time step 340 (*i.e.*, strain level of 44%). The analyses reported herein were carried out up to this point. On the deformed sample, the locations of buckling onset are highlighted by red rectangles, which corresponded to areas subjected to compression.

The carried out experiment with the anti-buckling fixture mostly resulted in negligible to small out-of-plane displacements. In Figure 3, out-of-plane displacement, residual and strain fields are reported for time step 340 before damage inception (Figure 2). The measured out-of-plane displacement field revealed a heterogeneous distribution, which indicated a tendency toward buckling. The area

of increased displacements denoted by the blue rectangle corresponds to zones where negative triaxialities were expected (*i.e.*, approximately -0.33, which indicates compressive stresses). The same area is not highlighted in the correlation residual map (Figure 3(b)), thus proving the trustworthiness of the measurements. Increased residuals were visible in the central part of the ROI (highlighted by the green rectangle). Due to the tendency toward buckling, minor wrinkling of the central part of the ROI occurred, which led to changes in brightness (*i.e.*, shadows). The strain map (Figure 3(c)) revealed that a single shear strain band developed between the V notches where the expected triaxiality was 0.

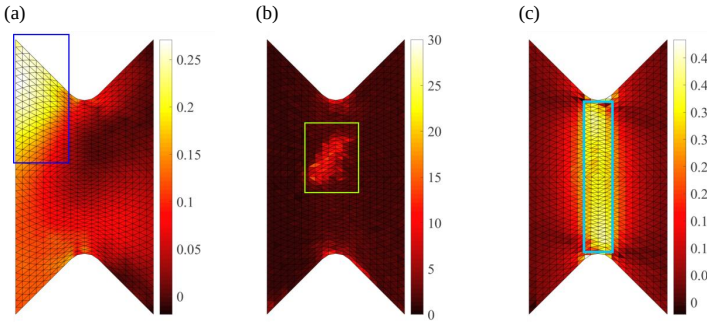

Fig. 3: (a) Out-of-plane Displacement (expressed in mm), (b) gray level residual (in % of the dynamic range of the reference images), and (c) ε_{12} strain fields for time step 340 (*i.e.*, before damage occurred). Positive displacements are oriented toward the reader. The blue box highlights localized increases in out-of-plane displacements where limited buckling initiated. The green box shows increased residuals where a slight change in brightness occurred. The cyan box depicts the location and size of the virtual strain gauge. Negligible out-of-plane displacements were measured and a uniform shear strain band developed.

3. Numerical protocol

In this section, the entire numerical protocol is presented. First, the FE models of the sample and the PMMA plates is introduced. Second, the five analyzed test

cases are defined. Last, the FEMU identification procedure is summarized. The numerical investigation presented herein dealt with the influence of the prescribed boundary conditions (BCs) on the predictions of the FE model, specifically the stress triaxiality fields. To evaluate the latter ones, the material parameters were calibrated via weighted Finite Element Model Updating (FEMU).

In the present analyses, the numerical simulations were driven by *experimentally measured* displacements prescribed as Dirichlet BCs. The goal was to analyze the influence of the BCs on the stress triaxiality fields. Yang *et al.* [68] introduced bifurcation analyses in FE simulations to analyze wrinkling of the modified Yoshida buckling test (YBT). Even though the numerical analyses closely followed the experiments, the BCs on the gripped part could not describe slip between the specimen and the grips in a straight forward manner. Using DIC measured data, there is no need to model the grips. Chen *et al.* [69] analyzed the influence of a disturbance force on buckling of YBT specimens. The simulation of thin sheet buckling was challenging, and imperfections had to be introduced in the numerical model. In the present study, the imperfections were included through the measured BCs. No geometrical imperfections were added [70]. All the reported simulations were performed with the implicit version of Abaqus [71], and no advanced tools (*e.g.*, arc length method or explicit schemes) were needed.

3.1. Test cases

Five distinct test cases (Figure 4) were defined for which the influence of BCs was evaluated on the stress triaxiality fields and sample buckling modeling (Table 3). For each studied case, the FE model of the sample was discretized with C3D8R elements.

3.1 Test cases

Table 3: Test cases with their boundary conditions

Test case	Description
T1	Measured U_x and U_y displacements on stressed surfaces and U_z displacements on the stressed edges of Surface 1 + PMMA plates ($\mu = 0.33$) (Figure 4(a) and (b) - R and Y)
T2	Measured U_x and U_y displacements on stressed surfaces and U_z displacements on the stressed edges of Surface 1 + PMMA plates ($\mu = 0.01$)
T3	Measured U_x and U_y displacements on stressed surfaces (Figure 4(b) - R)
T4	T3 and U_z displacements on stressed edges (Figure 4(b) - R and Y)
T5	T3 and U_z displacements on Surface 1 (Figure 4(b) - R, Y and B)

In test case T1 (Figure 4(a)), the assembly of the butterfly sample and the PMMA plates was modeled with defined interactions between the two parts. The measured displacements were prescribed on the stressed surfaces of the sample mesh as Dirichlet BCs. Out of plane (z) displacements were prescribed only along the stressed edges of Surface 1 whose normal was along negative z. Conversely, pure (*i.e.*, 2D) DIC displacements x and y were extruded through the thickness of the mesh (*i.e.*, along the z direction Figure 4(b) - denoted in Red and Yellow color).

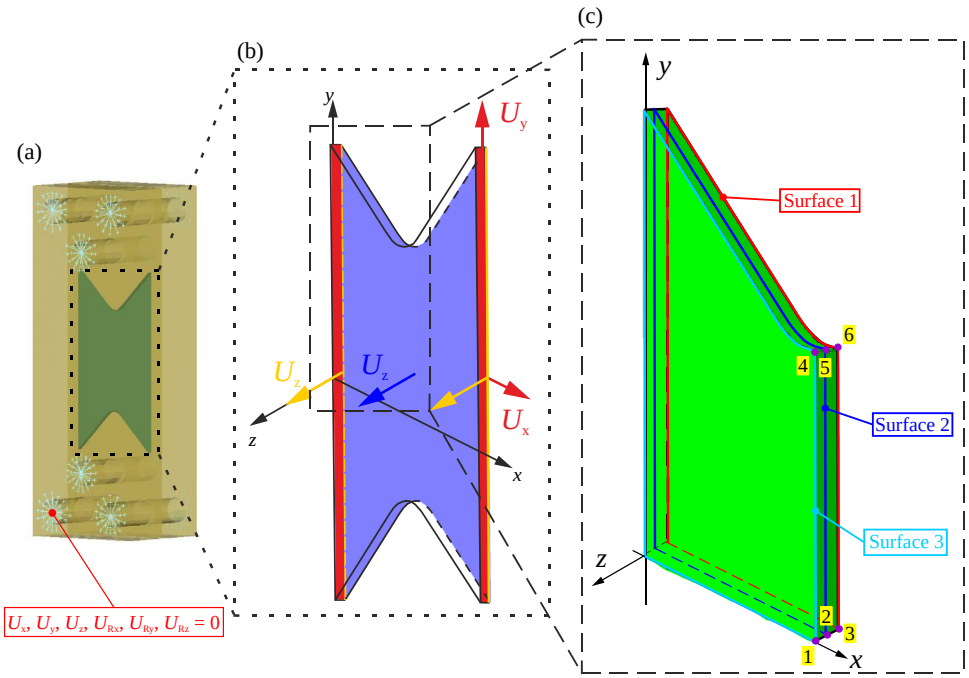

Fig. 4: (a) FE model with the PMMA plates. (b) Different sets of boundary conditions. Red (R) - in-plane displacements (U_x, U_y) on entire surfaces, yellow (Y) - out-of-plane displacements U_z on the edges and blue (B) - out-of-plane displacements U_z on the entire surface. (c) Detail of a quarter of the FE model where six points and three surfaces are defined, which are used for further analyses.

The second test case T2 was identical to T1 regarding the prescribed BCs and numerical model. However, the friction coefficient was set to $\mu = 0.01$ to probe the influence of negligible friction on the numerical model. For test case T3, only 2D displacements (*i.e.*, along x and y directions) were prescribed on the stressed surface (Figure 4(b) - denoted in Red color) as if they had been measured via 2D-DIC. This test case was not deemed eligible to simulate buckling as an idealized configuration was defined (*i.e.*, no imperfections in terms of out-of-plane displacements were introduced).

In test case T4, out-of-plane displacements were prescribed along the stressed edges of Surface 1, identical to T1 and T2, but the PMMA plates were not modeled (Figure 4(b) - denoted in Red and Yellow color). For the last test case (T5), the entire Surface 1 was further constrained with the measured out-of-plane-displacements (Figure 4(b) -denoted in Red, Yellow and Blue color). This choice was made due to the inaccurate description of buckling with case T4. To further probe the simulation validity regarding buckling, the out-of-plane displacements were prescribed on the entire surface. Each analysis performed herein was run for the first 340 time steps (*i.e.*, until the shear strain reached $\varepsilon_{12} = 0.44$, see Figure 2).

For the first two test cases, the interaction between the sample and the PMMA plates needed to be defined. General contact was introduced with Coulomb friction [72], where two different friction coefficients were considered. The plates were discretized with C3D4 tetrahedra. In the mechanical test, they were connected with six bolts that were not tightened. The numerical model was simplified to avoid modeling bolt pretension. The bolts were replaced by a combination of kinematic couplings and connector elements (CONN3D2, type = beam). Kinematic couplings were used to replace bolt heads on the surfaces around the holes (depicted by cyan lines in Figure 4(a)), whereas the connector elements represented the bolt shank and thread. Connector elements were used to link the master nodes of the kinematic coupling, thereby ensuring stiff connections between the plates. To prevent rigid body motions of the plates, for a single master node, all displacements and rotations were disabled (red dot in Figure 4(a)). For all other master nodes, only out-of-plane displacements were disabled. Elastic properties (*i.e.*, 3 GPa Young's modulus and 0.3 Poisson's ratio) were assigned to the PMMA

plates.

3.2. Parameter calibration

The extraction of stress triaxiality fields depends on material parameters. FEMU was employed as the identification procedure. To describe the nonlinear behavior, Armstrong-Frederick's kinematic hardening model [73] was selected. The sought parameters were the yield stress σ_y, hardening modulus C, and nonlinear coefficient c. FEMU minimizes differences between experimentally measured and numerically calculated quantities. The minimization procedure iteratively updates the sought parameters by calculating Hessian matrices based on sensitivity fields [49, 74] (*i.e.*, changes of each considered quantity for a small variation of the parameters). In the present cases, the differences between measured and computed displacement fields, as well as measured load and global reaction forces extracted from the numerical model were considered.

If the minimization procedure were to take into account only measured displacement fields (*i.e.*, FEMU-U), the cost function would be formulated as the sum of squared differences between measured $\{\mathbf{u}_m\}$ and computed $\{\mathbf{u}_c\}$ nodal displacements

$$\chi_u^2(\{\mathbf{p}\}) = \frac{1}{\gamma_u^2 N_u} \left\| \{\mathbf{u}_m\} - \{\mathbf{u}_c\} \right\|_2^2, \tag{1}$$

where $\{\mathbf{p}\}$ is the column vector gathering all sought material parameters, γ_u the standard displacement uncertainty, and N_u the number of kinematic degrees of freedom [74]. When the only source of error is due to the measurement uncertainty, χ_u tends to 1. Therefore, any deviation from 1 implies model errors.

FEMU may also be utilized to minimize the differences between the measured forces $\{\mathbf{F}_m\}$ and calculated reaction forces $\{\mathbf{F}_c\}$ (*i.e.*, FEMU-F) extracted from

the stressed edges of the FE model where Dirichlet BCs were prescribed

$$\chi_F^2(\{\mathbf{p}\}) = \frac{1}{\gamma_F^2 N_F} \left\| \{\mathbf{F}_m\} - \{\mathbf{F}_c\} \right\|_2^2, \tag{2}$$

where γ_F is the standard uncertainty of the load cell, and N_F the number of load data.

The identification procedure can be enhanced by combining the aforementioned cost functions

$$\chi_{tot}^2 = (1-\omega)\chi_u^2 + \omega\chi_F^2, \tag{3}$$

where the factor ω weighs the contribution of each individual cost function. In this work, ω was set to 0.5 to give equal weight to both cost functions.

4. Numerical results

In this section, the numerical results for each test case are presented and compared. First, FEMU was carried out to determine the optimal set of material parameters for each individual test case. For the identification procedure and further numerical analyses, the triangular T3 mesh used for stereocorrelation measurements (Figure 3) was converted into four-noded quadrilateral (Q4) elements. The 2D Q4 mesh was then extruded to construct the 3D mesh composed of linear brick elements with reduced integration (C3D8R).

4.1. FEMU identification results

The calibrated material parameters, their initial value and converged cost functions are gathered in Table 4. The parameters calibrated for test case T1 were used as initial guess for the other cases. For each test case, the elastic parameters (*i.e.*,

Young's modulus E and Poisson's ratio ν) were kept constant and set to 210 GPa and 0.25, respectively.

Table 4: FEMU results for all test cases. The calibrated parameters of case T1 were used as initial guess for all other test cases. Values of χ_U, χ_F and χ_{tot} are displayed for initial and converged solutions. The standard parameter uncertainties ($\pm$) are also indicated.

Parameter	σ_y, MPa	C, MPa	c	χ_U		χ_F		χ_{tot}	
				Initial	Converged	Initial	Converged	Initial	Converged
T1	360 ± 15	3860 ± 640	12 ± 1.7	60	59.6	40.4	9.3	51.2	42.6
T2	380 ± 9	3920 ± 460	11 ± 1.7	59.4	59.5	43.9	10.5	52.5	42.7
T3	380 ± 9	3920 ± 460	11 ± 1.7	34	33	44.4	10.4	32	24.5
T4	380 ± 10	3910 ± 510	11 ± 2	69	71	47	10.5	59	51
T5	380 ± 13	3890 ± 660	11 ± 2.4	7.8	7	45.8	10.7	32.9	9

The calibration procedure yielded parameters that provided good agreement between the measured load and the global reaction forces. Each calibration resulted in lowered global residual χ_{tot}. For case T1, the calibrated yield stress σ_y and hardening coefficient C were the lowest, except for the nonlinear coefficient c, which was the highest of all test cases. Furthermore, the converged global residual χ_{tot} and the force residual χ_F were lower compared to test cases T2 and T4.

The second test case T2 experienced an increase in yield stress σ_y by 6% and hardening coefficient C by 1%, whereas c was reduced by 7%. The global residual at convergence was only slightly higher than for T1. The displacement residuals for the initial parameters and at convergence displayed slightly lower values than their T1 counterpart. However, for T1 the force residuals were lower. Since friction was negligible, higher values of σ_y and C were calibrated to compensate for the additional force due to friction [63].

The third test case T3, where only in-plane measurements were prescribed,

yielded the second lowest global residual. This result was due to the lack of prescribed out-of-plane displacements that were affected by higher measurement uncertainties (Table 2). Furthermore, with this approach, buckling of the sample was not possible to simulate since no imperfections were considered. This observation highlights the significance of enriching the FE model with measured out-of-plane displacements for buckling simulation. Although only in-plane measurements were prescribed, it was decided to include out-of-plane displacements in the calculation of χ_{tot}, which was significantly lower than for test cases T1 and T2. This observation shows that prescribing only in-plane measurements was not sufficient to describe any out-of-plane motion. This test case cannot be considered representative of the real experiment since it was idealized. The identified values of the sought parameters were essentially the same as for test case T2 since no friction was included in the numerical model.

Even though the identification procedure converged, the global residual was the highest of all proposed FE modeling strategies for test case T4. Both displacement and force residuals for the first iteration and at convergence were greater than those for T1 and T2. Furthermore, the displacement residual experienced a slight increase at convergence due to higher out-of-plane displacements (*i.e.*, buckling, which could not be accurately described). It was concluded that 3D measurements prescribed as Dirichlet BCs were sufficient to simulate buckling. However, due to the complexity of the material behavior, buckling for case T4 was not fully controlled (*i.e.*, restricted by the PMMA plates). The deviation of the calculated out-of-plane displacements from the measured counterparts resulted in increased displacement residual χ_U. The initial and converged force residuals χ_F also displayed higher values than the previous test cases, except for T2 where the same

level was reached.

For the final test case T5, the measured out-of-plane displacements were prescribed over the entire Surface 1 to drive the numerical simulation toward limited buckling with Dirichlet BCs. The calculation of χ_U considered only stereocorrelation measurements. The lowest χ_{tot} was reached with this approach since out-of-plane displacements were accounted for and controlled. This last case resulted in approximately eight times lower displacement residuals than for T1. By constraining the entire Surface 1, buckling could be triggered with stereocorrelation data. The drawback of this approach is the introduction of additional measurement uncertainties in the prescribed out-of-plane displacements (Table 2). An additional cost function regarding the reaction forces extracted from the constrained surface was defined in the FEMU algorithm. The goal was to minimize these reaction forces to be as close as possible to zero. The identification procedure yielded the highest value of σ_y compared to all other test cases, which increased by approximately 7%, whereas C changed only slightly from its initial value (*i.e.*, 0.7%). The nonlinear coefficient c experienced the highest relative change (ca. 8%).

The standard uncertainty of the calibrated parameters was also calculated to determine the influence of the prescribed Dirichlet BCs. For the yield stress σ_y, the highest uncertainty was reached for test cases T1 and T5, *i.e.*, the more complex cases. The parameter uncertainties for the other three cases were similar. For test cases T1 and T5, the highest uncertainty for C was also observed, whereas for T2 and T3 they were similar. The highest uncertainty for c was obtained for case T5. From these results, it was concluded that the prescribed BCs had an influence on the calibrated material parameters. The most complex test cases T1 and T5 yielded the highest parameter uncertainties. For case T1, the cause was

friction, whereas for T5 it was due to the prescribed out-of-plane displacement on the entire measurement surface.

To illustrate the effect of friction, a *unique* set of material parameters was selected (*i.e.*, those of case T1, see Table 4) and computations were run with the five BCs. From each simulation, the reaction forces were extracted and are displayed in Figure 5(a). All test cases yielded lower reaction forces compared to T1. This trend was explained by the fact that all of them were frictionless (*i.e.*, for case T2 friction was approximately zero and for the other three it was not modeled). The influence of friction cannot be deemed negligible, which is further supported by the calibrated material parameters (Table 2). For the last four test cases, friction was neglected, and the FEMU procedure yielded higher values for σ_y and C compared to T1 to compensate for the absence of friction. This effect was especially apparent for the first two test cases T1 and T2 where the same numerical model was employed.

Cases T1 and T2 were very close in terms of numerical model. Their reaction force differences were the lowest of all the reported differences (Figure 5(b)), which was further substantiated by the lowest mean. The highest differences were observed between cases T1 and T4. Overall, the root mean square differences were about 33 times the standard force uncertainty γ_F. These results highlight the consequence of not including friction in the identification procedure.

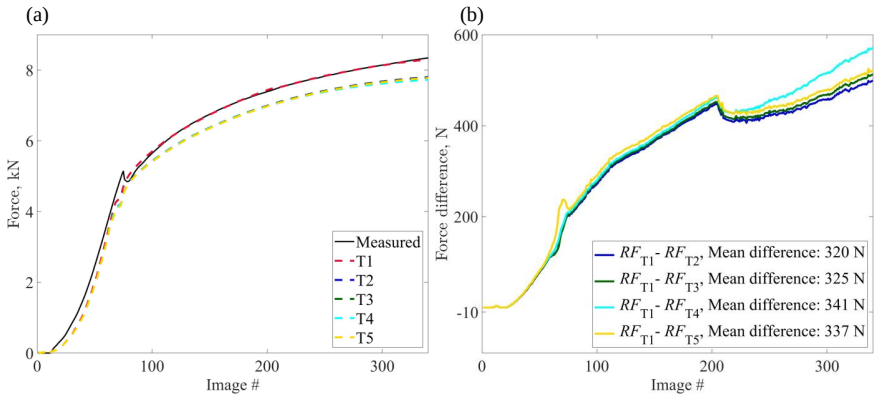

Fig. 5: (a) Comparison of global reaction forces extracted from the FE models for the material parameters calibrated for case T1. (b) Differences in global reaction forces with respect to T1. The mean reaction force differences were on average 33× higher than the standard force uncertainty γ_F ($i.e.$, $\chi_F \approx 33$). These results show the consequence of not including friction in the identification procedure (*i.e.*, lower reaction forces since the material parameters were not properly calibrated in the absence of friction).

4.2. *Stress triaxiality fields*

In the following, the influence of different BC prescriptions on stress triaxiality fields is studied, both surface-wise and node-wise (Figure 4(c)). Three surfaces were chosen to evaluate them, namely, the back Surface 1, middle Surface 2 and front Surface 3. Moreover, in total six nodes were chosen for the evaluation of the corresponding triaxialities. The three nodes in the middle (*i.e*, nodes 1, 2 and 3) of the FE model were chosen to asses the stress state in the gauge area (*i.e*, between the V notches) since the butterfly sample was designed to promote uniform stress states in the gauge region. The sample was subjected to simple shear, thus uniform shear stress states were expected (*i.e.*, the stress triaxiality should vanish). Furthermore, three points were chosen in the root of the V notch (*i.e*, nodes 4, 5 and 6) to evaluate the stress state in that area. All test cases

displayed similar distributions of stress triaxialities on the chosen sample planes (Figures 6-10). The locations of the initiated cracks in the sample (see inset of Figure 2) coincided with the areas of positive stress triaxialities (*i.e.*, ≈ 0.33) where tensile stresses occurred.

From the stress triaxiality fields shown in Figure 6 for test case T1, identical distributions are observed on all three surfaces. The stress triaxiality fields were generally divided into three main parts, namely, areas with positive (red) tensile, negative (blue) compressive, and approximately zero (green) shear parts. Small fluctuations in terms of increased stress triaxiality values occurred on the edges of the surfaces. This effect was attributed to the prescribed BCs, which introduced additional random fluctuations due to measurement uncertainties. Furthermore, no severe wrinkling was caused by sample buckling since it was prevented with this numerical model.

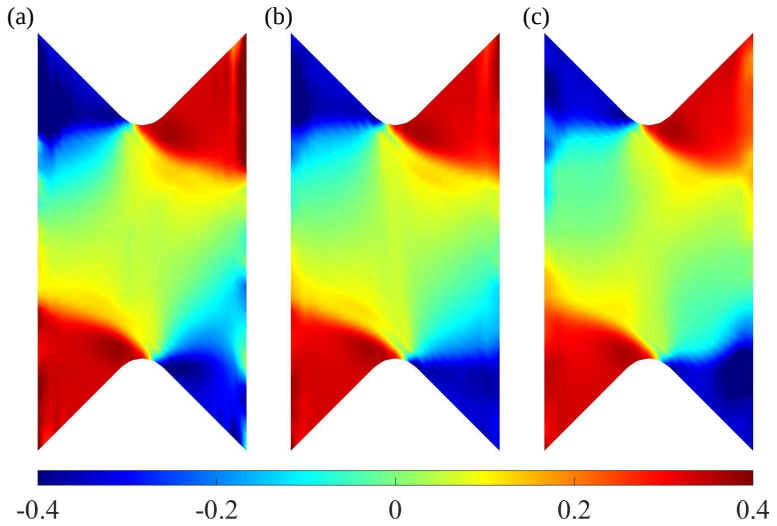

Fig. 6: Stress triaxiality fields for time step 340 (test case T1), for the front surface (a), the mid-thickness surface (b) and back surface (c). Almost identical fields are observed for the three analyzed surfaces.

Test case T2 (Figure 7) displayed identical triaxiality distributions as T1 since the numerical model was the same, except for the value of the friction coefficient. As in the previous case, increased stress triaxiality levels were observed on the boundaries of the FE model where Dirichlet BCs were prescribed. The stress triaxiality in the middle of the gauge area was also close to zero. From the stress triaxiality fields, it was concluded that the influence of friction remained very limited.

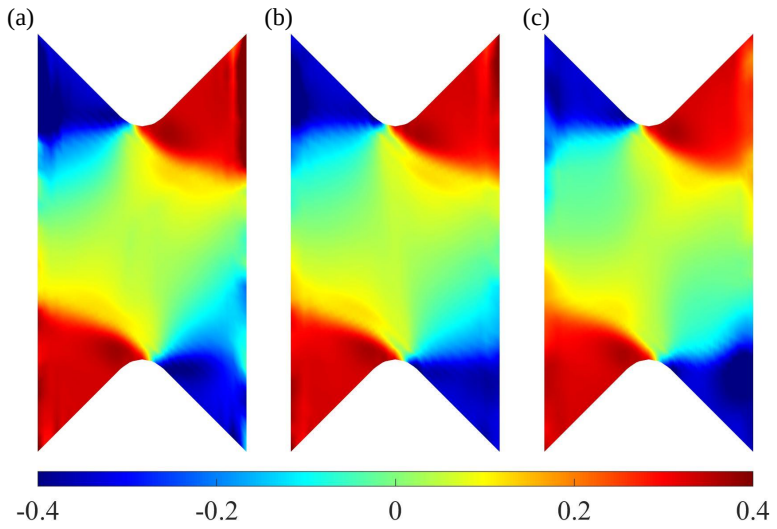

Fig. 7: Stress triaxiality fields for time step 340 (test case T2), for the front surface (a), the mid-thickness surface (b) and back surface (c). Almost identical fields are observed for the three analyzed surfaces.

Test case T3 differed from other ones as it was the only configuration where no out-of-plane displacements were prescribed to the FE model. No buckling developed in the numerical simulations since they were idealized (*i.e.*, there were no imperfections in terms of out-of-plane displacement). All three surfaces displayed identical stress triaxiality distributions. The stress triaxiality levels in the middle of the gauge area were close to zero (*i.e.*, a shear stress state developed). Similar

distributions of stress triaxialities were observed compared to cases T1 and T2, and the constrained edges of the FE model displayed lower fluctuations since no out-of-plane displacements were prescribed.

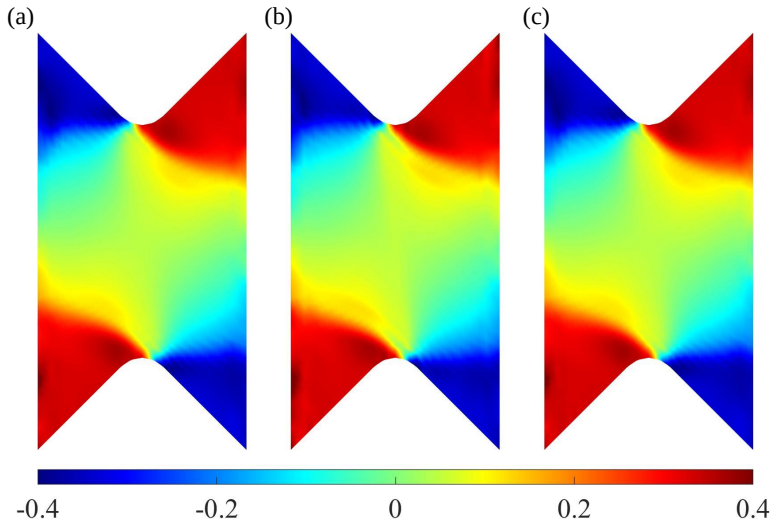

Fig. 8: Stress triaxiality fields for time step 340 (test case T3), for the front surface (a), the mid-thickness surface (b) and back surface (c). Almost identical fields are observed for the three analyzed surfaces.

For test case T4, the fluctuations in the stress triaxiality fields on Surfaces 1 and 3 (Figure 9) were more marked. The middle Surface 2 was similar to the previous test cases and no significant fluctuations occurred. However, Surface 1 suffered from more important variations in the stress triaxiality field in the middle of the gauge section, where zero levels were expected. This effect was attributed to buckling, which was triggered by introducing out-of-plane displacements in the Dirichlet BCs. Even though buckling developed, it was not severe. Its influence on the stress triaxiality fields was not negligible since additional stresses were induced. From the stress triaxiality fields, the effect of limited buckling was seen. The gauge area on Surface 1 was subjected to tensile stresses, whereas the same

area on Surface 3 was compressed. From this observation, it was concluded that buckling was oriented away from the reader.

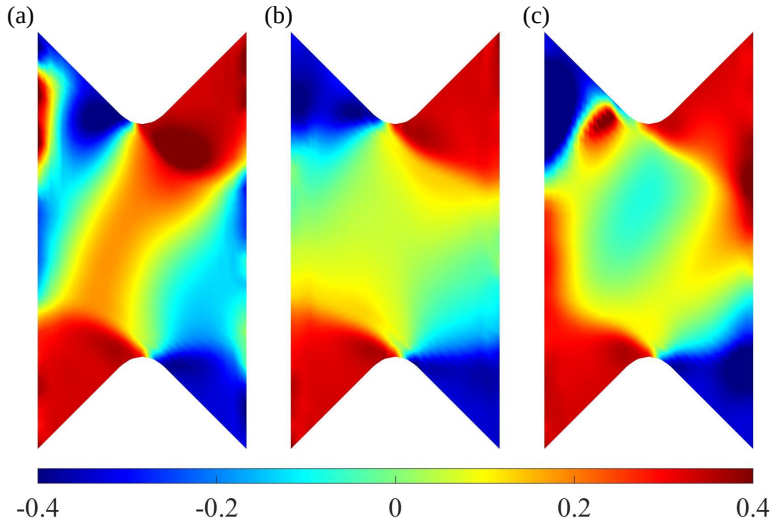

Fig. 9: Stress triaxiality fields for time step 340 (test case T4), for the front (a) and back (c) surfaces where the influence of buckling is more pronounced than for the mid-thickness surface (b).

Since the entire Surface 1 was constrained by the prescribed out-of-plane displacements, test case T5 was the most sensitive to measurement uncertainties. Triaxiality fluctuations were observed on all three surfaces in Figure 10, and as expected, Surface 1 was most affected. The stress triaxiality distribution on all three surfaces was still close to the previous cases. For test case T4, where buckling was also simulated, similar distributions of stress triaxialities in the gauge region were distinguished. The stress triaxiality values for the red areas ranged from 0.3 to approximately 0.5, which was similar to the levels obtained for cases T1 and T2. In the gauge area, they were higher than for T1. This trend was attributed to buckling inception since out-of-plane displacements were prescribed on Surface 1.

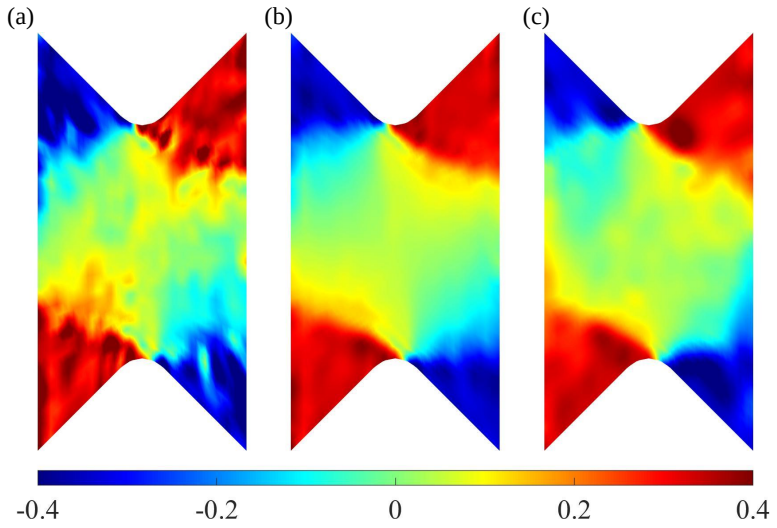

Fig. 10: Stress triaxiality fields for time step 340 (test case T5). For the front surface (a), the influence of the measurement uncertainties is more important than for the back surface (c); for the mid-thickness surface (b) it is minimal.

The stress triaxiality history for the six chosen nodes (Figure 4(c)) is plotted against the average shear strain calculated from the virtual gauge (Figure 3(c)) and reported in Figure 11. From the analysis of the stress triaxiality fields, it was concluded that the gauge area was subjected to predominantly shear stresses (*i.e.*, with stress triaxiality approximately equal to zero). The middle nodes 1, 2 and 3 (Figure 3(a)) for case T1 (Figure 11(a)) displayed small deviations through the thickness in the middle of the sample with an increase of the mean shear strain. However, the mean values for time step 300 were equal to 0.03 for all three nodes (Table 5). The second set of nodes (*i.e.*, 4, 5 and 6) experienced notable fluctuations. However, their levels all converged toward 0.33 (*i.e.*, tensile stress state) for the final time step.

Table 5: Mean nodal stress triaxiality for each test case in the plastic regime (*i.e.*, from time step 100 to 340)

Node	1	2	3	4	5	6
T1	0.01	0.02	0.03	0.20	0.19	0.20
T2	0.01	0.02	0.03	0.20	0.19	0.20
T3	0.02	0.02	0.02	0.20	0.19	0.20
T4	-0.01	0.02	0.06	0.20	0.20	0.25
T5	0.01	0.02	0.04	0.20	0.25	0.50

Test case T2 was essentially identical to T1 with regards to nodal stress triaxiality history, thereby indicating negligible influence of friction on the stress triaxiality (Figure 11(b)). Furthermore, similarities were also observed for the mean levels (Table 5); for cases T1, T2 and T3, they were identical. Test case T3, where only in-plane displacements were prescribed on the stressed edges, did not exhibit any buckling, which was further illustrated by the indistinguishable stress triaxiality histories for nodes 1, 2 and 3 and 4 and 6 (Figure 11(c)). Node 5 displayed an identical history as cases T1 and T2.

Test case T4, where the FE model was enriched with out-of-plane displacements, exhibited more pronounced buckling compared to the first two cases (Figure 11(d)). Therefore, the previously commented trend for nodes 1,2 and 3 was no longer observed. A divergence of nodal stress triaxialities occurred (Figure 11(d)). This phenomenon was attributed to buckling since Surface 3 (Node 1) was subjected to compression and Surface 1 (Point 3) to tension according to the stress triaxiality fields (Figure 9). The middle point 2 displayed the same response as in

previous test cases. Nodes 4 and 6 also experienced higher divergence compared to the other test cases. Nodes 2 and 5 located on the middle plane (*i.e.*, Surface 2) did not exhibit any dependence on buckling as the levels and histories were equivalent to case T1.

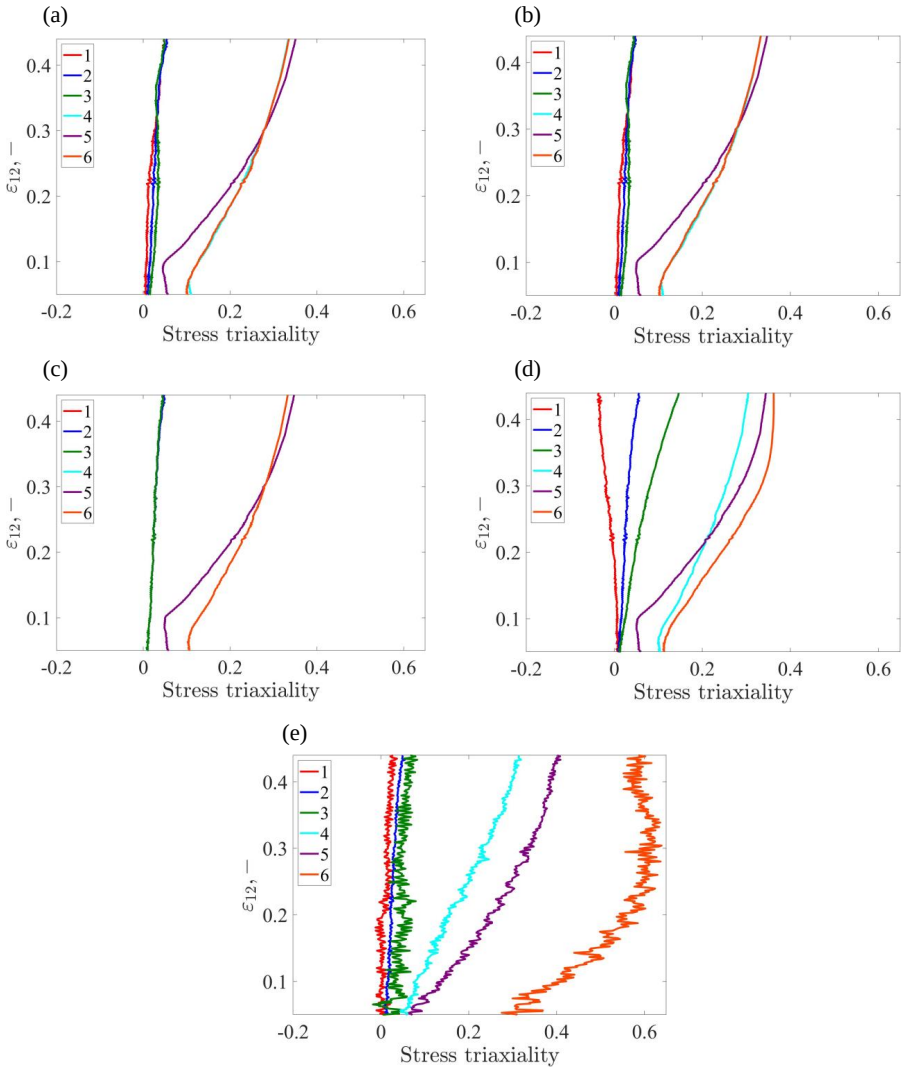

Fig. 11: Nodal stress triaxiality history vs. mean shear strain (in the optical gauge) for test cases T1 (a), T2 (b), T3 (c), T4 (d) and T5 (e). For the middle nodes 1,2 and 3, the trend is similar for all cases, except T4 where buckling developed. For nodes 4, 5 and 6 the trend is similar for each test case.

The introduction of measured out-of-plane displacements on Surface 1 resulted in noisier stress triaxialities (Figure 11(e)). Although all nodes were affected, nodes 3 and 6 suffered the most since they were located on the constrained surface, thus displaying higher sensitivity to measurement uncertainties. The influence of the latter ones was also observed from the mean values of all nodes as they showed slight deviations from the previous test cases, especially for node 6, which was two times higher than for the other cases (Table 5).

Figure 12 reports the mean stress triaxiality differences for Surface 2 with respect to test case T1 since for the chosen plane all cases displayed similar results. The mean stress triaxiality differences for test cases T2 and T4 showed similar trends. For the first one hundred images (in elasticity) the differences were insignificant, whereas in the plastic regime they were several orders of magnitude larger. Conversely, test cases T3 and T5 exhibited much larger differences than T2 and T4 in elasticity. However, T3 did not display any distinct change in the difference levels, whereas T5 showed a gradual decrease of the differences with increased load levels. This trend was attributed to a better description of sample buckling, thus better simulating the complex stress states in the material. Although additional measurement uncertainties were introduced in test case T5, no severe anomalies were observed. In plasticity, the mean differences for all test cases were of similar order of magnitude.

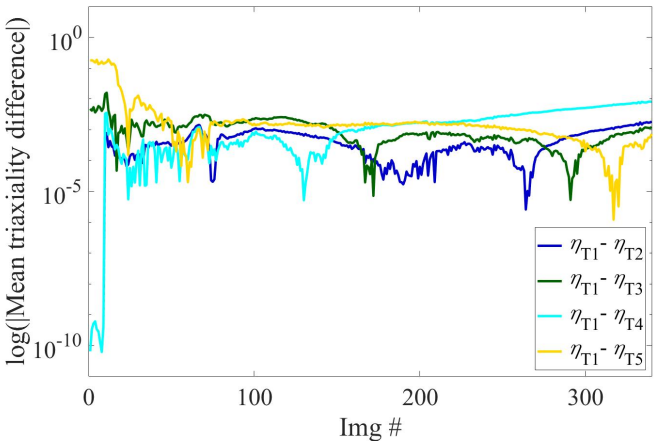

Fig. 12: Comparison of mean stress triaxiality differences for Surface 2 between all test cases with respect to T1. Highest differences are reported in elasticity, whereas for plasticity the differences are of similar orders of magnitude. Slightly higher differences are observed between test cases T1 and T4 thereby confirming that for the stress triaxiality fields it is necessary to use a 3D model.

5. Discussion

In this section, the influence of the calibrated parameters on the stress triaxiality fields is studied for each test case. The converged solution for the stress triaxiality fields was subtracted to that for which a single parameter was changed by 1%. The standard differences per image are displayed for all three surfaces to study the influence of the considered parameter through the sample thickness.

By observing the standard sensitivity to the yield stress σ_y (Figure 13), a sudden increase to stress triaxiality differences occurred in the early stages of yielding as seen on the force curve. This trend was similar in all test cases. For cases T1 and T5, the increase was more pronounced than for the other ones. In the middle of the sample (*i.e.*, Surface 2) the highest difference was observed for T1, whereas on Surface 3 it was for cases T5 and T1. This trend was attributed to the complex-

ity of the numerical models. After the initial stages of yielding, the calculated differences were lower and stable until the end of the numerical analysis.

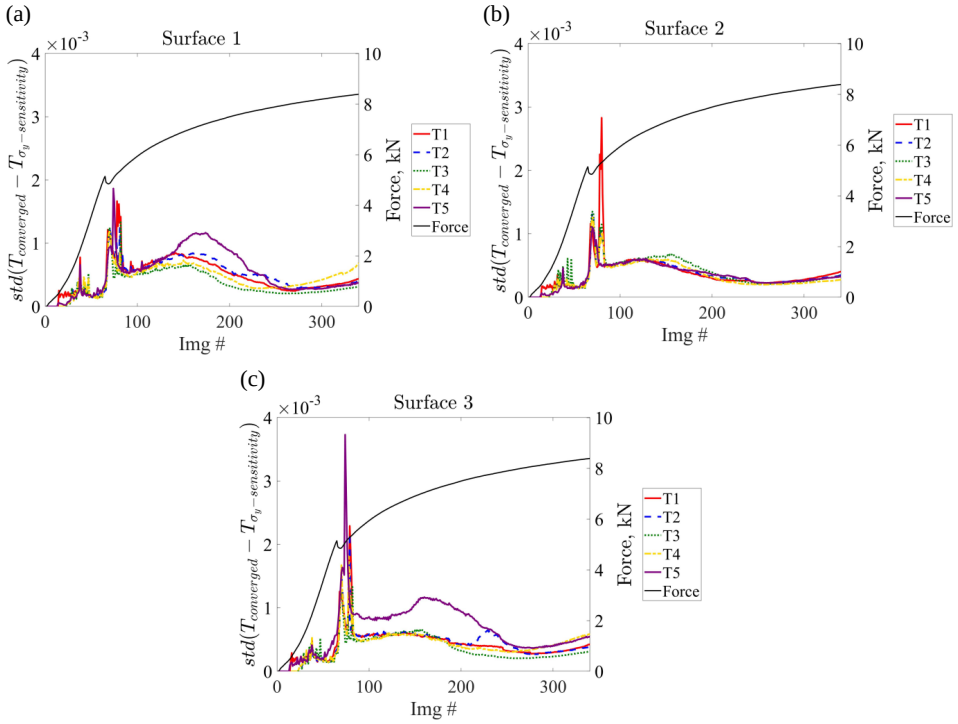

Fig. 13: Standard sensitivity of stress triaxiality fields to σ_y for each test case for (a) Surface 1, (b) Surface 2 and (c) Surface 3. A sudden increase in standard sensitivity occurred in the early stages of yielding for each test case. These changes are negligible since they were two orders of magnitude lower than the actual stress triaxiality levels.

The standard sensitivity of the stress triaxiality fields to parameter C (Figure 14) was the highest in the early stages of hardening. In elasticity and early plasticity, they were negligible and after yielding they began to rise. After the maximum point, the values decreased and remained low until the end of the numerical simulations. For case T5, the highest level was reached for Surfaces 1 and 3. For Surface 2, all test cases displayed similar values. However, for Surfaces 1 and 3, T4 was an outlier since toward the end of the simulation the stress

triaxiality differences did not follow the same trend as the other test cases.

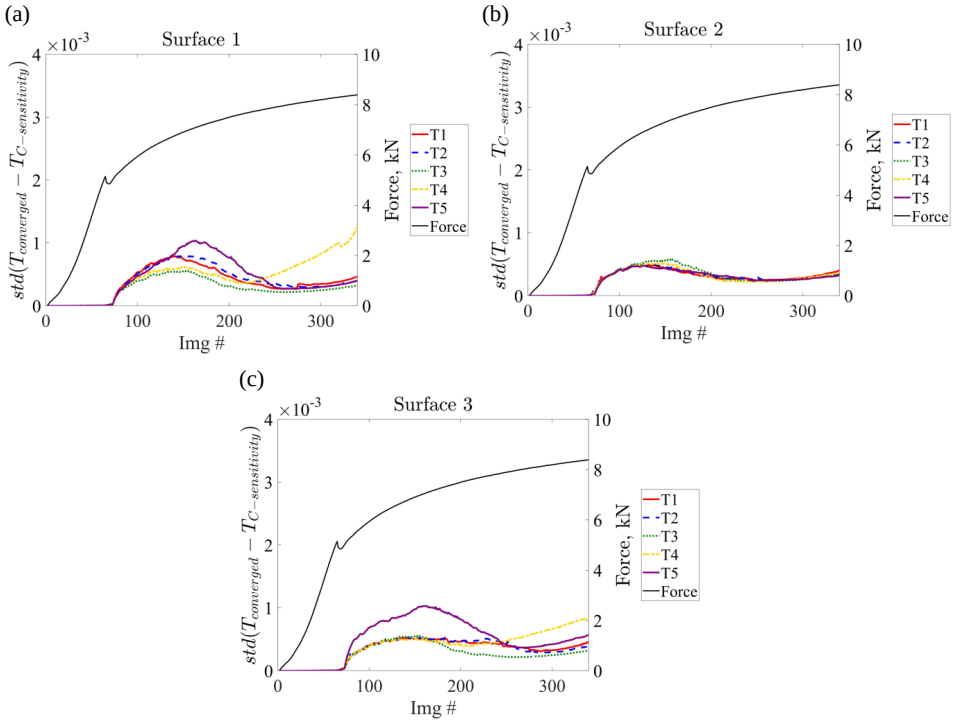

Fig. 14: Standard sensitivity of stress triaxiality fields to parameter C for each test case for (a) Surface 1, (b) Surface 2 and (c) Surface 3. The standard sensitivities were higher in early plasticity. Such changes are negligible since they are approximately three orders of magnitude lower than the actual stress triaxiality levels.

For all test cases, the change in parameter c (see Figure 15) displayed an influence on the stress triaxiality differences at the very end of the numerical simulations (*i.e.*, when approaching the ultimate load). In elasticity and early plasticity, the differences were negligible. During the early stages of hardening the influence was more noticeable. Yet, it was still limited in comparison to later stages. On Surface 1, case T4 displayed much higher values than the other ones due to buckling initiation.

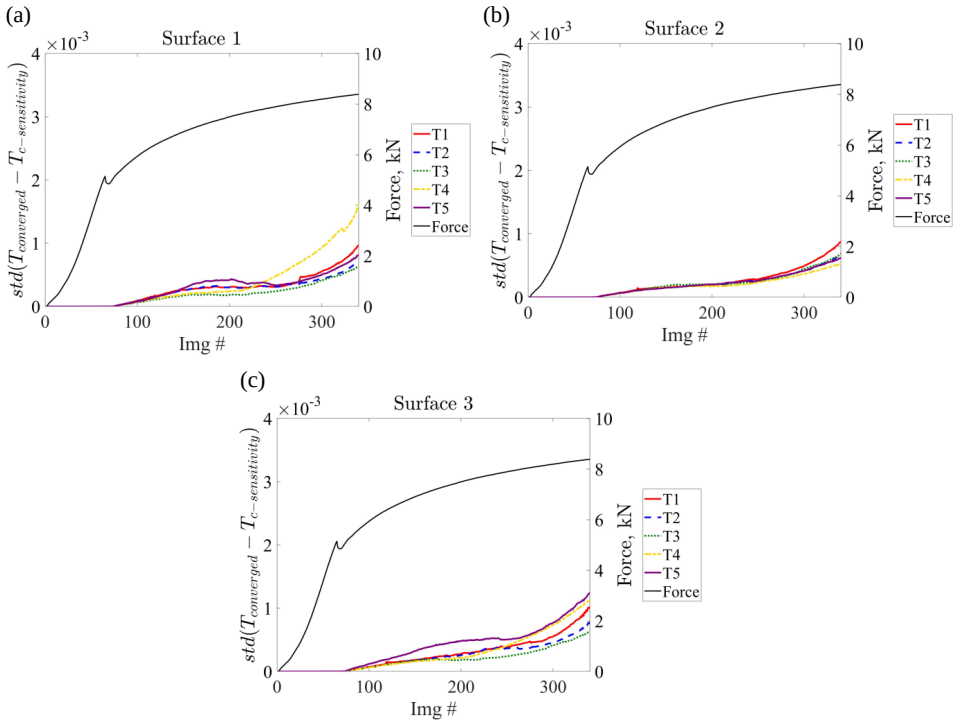

Fig. 15: Standard sensitivity of stress triaxiality fields to parameter c for each test case for (a) Surface 1, (b) Surface 2 and (c) Surface 3. The standard sensitivities are more pronounced at the very end of the numerical simulations. These changes are negligible (three orders of magnitude lower) compared to the actual triaxiality levels.

From Figures 13-15 it was concluded that the change in triaxiality fields remained very limited as the standard variations were of the order of 10^{-3}. These differences were ten times lower than the parameter changes. It is worth noting that for Surface 2, for each parameter, the stress triaxiality differences were minimal and the curves for each test case were in good agreement. For the yield stress σ_y, the differences were higher in amplitude than for the hardening parameters C and c for each test case and surface.

Table 6 gathers the mean sensitivities calculated from image 150 until the end of the analysis for each surface and test case observed in Figures 13-15. For Sur-

faces 1 and 3, larger fluctuations were observed, where T5 displayed the highest sensitivity to material parameter changes. Conversely, for Surface 2, the change of material parameters induced similar influences on the stress triaxiality changes for each test case. These values were two orders of magnitude lower than the parameter change (1%).

Table 6: Mean standard sensitivities to parameter changes for the three considered surfaces

	$\overline{std(\sigma_y)} \times 10^{-4}$			$\overline{std(C)} \times 10^{-4}$			$\overline{std(c)} \times 10^{-4}$		
	S1	**S2**	**S3**	**S1**	**S2**	**S3**	**S1**	**S2**	**S3**
T1	3.9	3.1	4.4	4.2	3.1	4.2	4.3	3.5	4.2
T2	4.3	3.2	4.9	4.1	3.1	4.5	3.7	3.1	3.7
T3	3.1	3.4	3.1	3	3.2	3	2.9	3.1	2.9
T4	4.2	2.9	4.4	5.4	3	6.2	4.7	2.7	5.8
T5	6.7	3.2	5.8	6.2	3	5.3	6.1	3	4.4

Last, the comparison between all test cases is analyzed. Test case T5 was taken as reference and the stress triaxiality fields were subtracted to each previous test case only for Surface 1. This choice was made as measured out-of-plane displacements were prescribed on the aforementioned surface. Root mean square (RMS) differences were calculated and are displayed in Figure 16. It was observed that in elasticity, the RMS differences were about eight times higher than in the hardening stages of the sample (Figure 16(a)). In the semi-logarithmic plot (Figure 16(b)) this trend becomes clearer. In elasticity, each type of BC had a strong influence on the stress triaxiality levels and distributions. As plasticity set in, the displacement levels became higher. Therefore, when comparing these computations, the results

in elasticity were discarded.

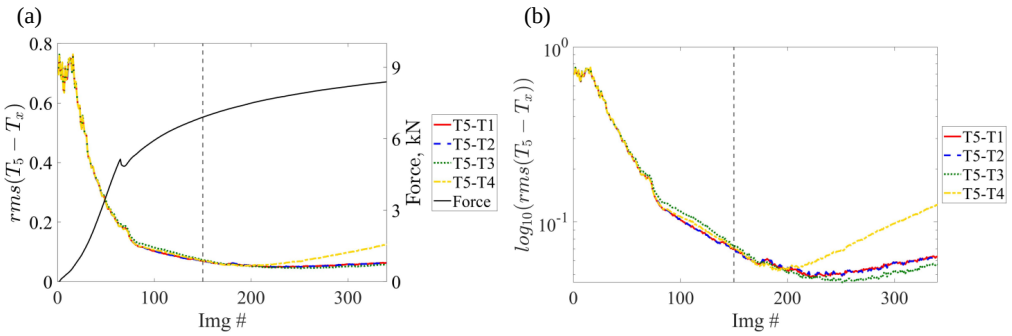

Fig. 16: Root mean square differences in stress triaxiality fields with respect to test case T5 for Surface 1. (a) RMS difference vs. image number. (b) Semi-logarithmic plot of the previous differences. The dashed vertical line depicts the beginning of the computations reported in Table 7. The highest differences are for case T4 where buckling developed whereas for other cases they remained of same order of magnitude.

In Table 7, the mean values of the RMS differences are gathered from image 150 until the final one. It was observed that the lowest value was for T3. Since T1 and T2 were similar, except for the consideration of friction, the mean differences were close. The highest difference was for case T4, where significant and unphysical buckling occurred. Although there was a visible influence of different BCs, they remained low.

Table 7: Mean RMS differences in stress triaxiality fields with respect to T5 for Surface 1

Case	$\overline{RMS}$
T5-T1	0.0561
T5-T2	0.0563
T5-T3	0.0528
T5-T4	0.0768

6. Conclusions and outlook

In this study, an extensive analysis was carried out to evaluate the effect of different Dirichlet BCs on the evaluation stress triaxiality fields. The prescribed displacements were measured via FE-based stereocorrelation for a simple shear test on a 1 mm thick sample. To evaluate stress triaxiality fields, the constitutive equation and its parameters had to be identified. Armstrong-Frederick's kinematic hardening model was selected and calibrated via weighted FEMU.

First, the five investigated cases led to different sets of material parameters. Yet, negligible influence was evidenced on the stress triaxiality fields. A very fine calibration of the material response was thus not required in the studied test.

Second, when modeling the anti-buckling fixture, the friction coefficient was considered as an additional parameter to be calibrated. Compared to the predictions with a very small value, the stress triaxiality fields were very close even though the calibrated material responses were different. Such simulations were very costly, therefore three other cases were also investigated.

Third, by prescribing only in-plane displacements measured on the stressed surfaces of the FE model, limited wrinkling was not accounted for. Interestingly, the stress triaxiality fields were close to the previous estimates and constituted a first estimate if wrinkling had been fully prevented.

Fourth, by also considering the out-of-plane displacements on the stressed edges of the sample, buckling was observed in the simulations. The resulting deformed shape was not consistent with the measured one. Different stress triaxiality fields were observed and it was concluded that they were not physical.

Fifth, prescribing all out-of-plane displacements as BCs on the sample surface,

limited buckling was accurately simulated. The drawback was the inclusion of additional measurement uncertainties through such BCs. As a result, the stress triaxiality fields were more fluctuating, yet close to the levels observed when modeling the anti-buckling fixture. This case provided, by construction, accurate deformed shapes in a less computationally demanding manner than the first one.

The framework presented herein is not limited to the specific experiment where simple shear was applied to an Arcan sample. The procedure is generic and may also be applied to simpler or more complex experimental investigations and for other materials.

Acknowledgements

This work was performed within the FULLINSPECT project supported by the Croatian Science Foundation (UIP-2019-04-5460 Grant). The authors also acknowledge and thank EikoSim for providing the EikoTwin DIC software to perform the stereocorrelation analysis reported herein.

Compliance with Ethical Standards

The authors have no conflict of interest to declare.

References

[1] Tekkaya AE, Allwood JM, Bariani PF, Bruschi S, Cao J, Gramlich S, Groche P, Hirt G, Ishikawa T, Löbbe C, Lueg-Althoff J, Merklein M, Misiolek WZ, Pietrzyk M, Shivpuri R, Yanagimoto J (2015) Metal forming beyond shaping: Predicting and setting product properties. CIRP Ann - Manuf Technol 64(2):629–653, 10.1016/j.cirp.2015.05.001

[2] Bae DG, Ghosh AK (2000) A planar simple shear test and flow behavior in a superplastic Al-Mg alloy. Metall Mater Trans A 34:2465–2471

[3] Driemeier L, Brünig M, Micheli G, Alves M (2010) Experiments on stress-triaxiality dependence of material behavior of aluminum alloys. Mech Mater 42:207–217, 10.1016/j.mechmat.2009.11.012

[4] Zhang K, Badreddine H, Hfaiedh N, Saanouni K, Liu J (2021) Enhanced CDM model accounting of stress triaxiality and Lode angle for ductile damage prediction in metal forming. Int J Damage Mech 30(2):260–282, 10.1177/105678952095804

[5] Sutton M, Wolters W, Peters W, Ranson W, McNeill S (1983) Determination of displacements using an improved digital correlation method. Image Vis Comput 1(3):133–139, 10.1016/0262-8856(83)90064-1

[6] Sutton M, McNeill S, Helm J, Chao Y (2000) Advances in two-dimensional and three-dimensional computer vision. In: Rastogi P (ed) Photomechanics, Springer, Berlin (Germany), vol Topics in Appl. Phys., 77, pp 323–372

[7] Hild F, Roux S (2006) Digital image correlation: From measurement to identification of elastic properties - a review. Strain 42:69–80

[8] Pan B, Qian K, Xie H, Asundi A (2009) Two-dimensional digital image correlation for in-plane displacement and strain measurement: a review. Measurement Science and Technology 20(6):062001, 10.1088/0957-0233/20/6/062001

[9] Sutton M (2013) Computer vision-based, noncontacting deformation measurements in mechanics: A generational transformation. Applied Mechanics Reviews 65(AMR-13-1009):050802

[10] Sutton M, Hild F (2015) Recent advances and perspectives in digital image correlation. Experimental Mechanics 55(1):1–8

[11] Sun Y, Pang J, Wong C, Su F (2005) Finite-element formulation for a digital image correlation method. Applied Optics 44(34):7357–7363

[12] Besnard G, Hild F, Roux S (2006) "Finite-element" displacement fields analysis from digital images: Application to Portevin-Le Chatelier bands. Experimental Mechanics 46:789–803

[13] Hild F, Roux S (2012) Comparison of Local and Global Approaches to DIC. Exp Mech 52(9):1503–1519, 10.1007/s11340-012-9603-7

[14] Wang B, Pan B (2016) Subset-based local vs. finite element-based global digital image correlation: A comparison study. Theor Appl Mech Lett 6(5):200–208, 10.1016/j.taml.2016.08.003

[15] Lou Y, Chen L, Clausmeyer T, Tekkaya A, Whan Yoon J (2017) Modeling of ductile fracture from shear to balanced biaxial tension for sheet metals. Int J Solids Struct 112:169–184, 10.1016/j.ijsolstr.2016.11.034

[16] Yu F, Ben Jar P, Hendry M (2018) Constitutive analysis of pressure-insensitive metals under axisymmetric tensile loading: A stress triaxiality-dependent plasticity damage model. Int J Mech Sci 142–143:21–32, 10.1016/j.ijmecsci.2018.04.035

[17] Peng J, Wang Y, Dai Q, Liu Y, Liu L, Zhang Z (2019) Effect of Stress Triaxiality on Plastic Damage Evolution and Failure Mode for 316L Notched Specimen. Metals 9(1067):1–18, 10.3390/met9101067

[18] Rickhey F, Hong S (2022) Stress Triaxiality in Anisotropic Metal Sheets—Definition and Experimental Acquisition for Numerical Damage Prediction. Materials 15(11):3738, 10.3390/ma15113738

[19] Wang S, Wang Y, Yu L, Ji K, Liu X, Lou Y (2022) Failure Modeling for QP980 Steel by a Shear Ductile Fracture Criterion. Metals 12(452):1–18, 10.3390/met12030452

[20] Djaziri S, Renault P, Hild F, Le Bourhis E, Goudeau P, Thiaudière D, Faurie D (2011) Combined synchrotron x-ray and image-correlation analyses of biaxially deformed w/cu nanocomposite thin films on kapton. J Appl Crystallogr 44:1071–1079, 10.1107/S0021889811030226

[21] Djaziri S, Faurie D, Le Bourhis E, Goudeau P, Renault P, Mocuta C, Thiaudière D, Hild F (2013) Deformation modes of nanostructured thin film under controlled biaxial deformation. Thin Solid Films 530:30–34, 10.1016/j.tsf.2012.05.051

[22] Güner A, Zillmann B, Lampke T, Tekkaya AE (2014) In-situ Measurement of Loading Stresses with X-ray Diffraction for Yield Locus Determination. Int J Automot Technol 15(2):303–316, 10.1007/s12239-014-0031-9, http://link.springer.com/article/10.1007/s12239-012-0027-2

[23] Voillot B, Lebrun JL, Billardon R, Hild F (2018) Validation of registration

techniques applied to XRD signals for stress evaluations in titanium alloys. Experimental Mechanics 58(8):1265–1280, 10.1007/s11340-018-0391-6

[24] Réthoré J (2017) Computational measurements of stress fields from digital images. Int J Numer Methods Eng 113(12):1810–1826, https://doi.org/10.1002/nme.5721

[25] Dalémat M, Coret M, Leygue A, Verron E (2019) Measuring stress field without constitutive equation. Mech Mater 136, 10.1016/j.mechmat.2019.103087

[26] Musiał S, Nowak M, Maj M (2019) Stress field determination based on digital image correlation results. Arch Civ Mech Eng 19(4):1183–1193, 10.1016/j.acme.2019.06.007

[27] Andrade F, Conde S, Feucht M, Helbig M, Haufe A (2019) Estimation of Stress Triaxiality from optically measured Strain Fields. In: 12th European LS-DYNA Conference, 1

[28] Brosius A, Küsters N, Lenzen M (2018) New method for stress determination based on digital image correlation data. CIRP Ann 67(1):269–272, 10.1016/j.cirp.2018.04.026

[29] Lindner D, Mathieu F, Hild F, Allix O, Minh CH, Paulien-Camy O (2015) On the evaluation of stress triaxiality fields in a notched titanium alloy sample via integrated digital image correlation. J Appl Mech Trans ASME 82(7):1–10, 10.1115/1.4030457

[30] Abushawashi Y, Xiao X, Astakhov V (2013) A novel approach for determining material constitutive parameters for a wide range of triaxiality under plane strain loading conditions. Int J Mech Sci 73:133–142, 10.1016/j.ijmecsci.2013.05.007

[31] Barsoum I, Faleskog J, Pingle S (2012) The effect of stress state on ductility in the moderate stress triaxiality regime of medium and high strength steels. Int J Mech Sci 65:203–212, 10.1016/j.ijmecsci.2012.10.003

[32] Anderson D, Winkler S, Bardelcik A, Worswick M (2014) Influence of stress triaxiality and strain rate on the failure behavior of a dual-phase DP780 steel. Mater Des 60:198–207, 10.1016/j.matdes.2014.03.073

[33] Brünig M, Brenner D, Gerke S (2015) Stress state dependence of ductile damage and fracture behavior: Experiments and numerical simulations. Eng Frac Mech 141:152–169, 10.1016/j.engfracmech.2015.05.022

[34] Brünig M, Gerke S, Zistl M (2019) Experiments and numerical simulations with the H-specimen on damage and fracture of ductile metals under non-proportional loading paths. Eng Frac Mech 217:106531, 10.1016/j.engfracmech.2019.106531

[35] Gerke S, Adulyasak P, Brünig M (2017) New biaxially loaded specimens for the analysis of damage and fracture in sheet metals. Int J Solids Struct 110–111:209–218, 10.1016/j.ijsolstr.2017.01.027

[36] Brünig M, Zistl M, Gerke S (2020) Biaxial experiments on characterization of stress-state-dependent damage in ductile metals. Prod Eng 14:87–93, 10.1007/s11740-019-00930-2

[37] Zistl M, Brünig M, Gerke S (2022) Analysis of damage and fracture behavior in ductile metal sheets undergoing compression and shear preloading. Int J Mater Form 15(59):1–14, 10.1007/s12289-022-01705-4

[38] Huang J, Guo Y, Qin D, Zhou Z, Li D, Li Y, Li Y (2018) Influence of stress triaxiality on the failure behavior of Ti-6Al-4V alloy under a broad range of strain rates. Theor Appl Fract Mech 97:48–61, 10.1016/j.tafmec.2018.07.008

[39] Wang B, Xiao X, Astakhov V, Liu Z (2019) The effects of stress triaxiality and strain rate on the fracture strain of Ti6Al4V. Eng Frac Mech 219:106627, 10.1016/j.engfracmech.2019.106627

[40] Peng J, Zhou P, Wang Y, Dai Q, Knowles D, Mostafavi M (2021) Stress Triaxiality and Lode Angle Parameter Characterization of Flat Metal Specimen with Inclined Notch. Metals 10(11):1627, 10.3390/met11101627

[41] Pham VV, Nguyen VC, Tounsi A (2022) Static bending and buckling analysis of bi-directional functionally graded porous plates using an improved first-order shear deformation theory and FEM. Eur J Mech A/Solids 96:104743, 10.1016/j.euromechsol.2022.104743

[42] Avril S, Bonnet M, Bretelle A, Grédiac M, Hild F, Ienny P, Latourte F, Lemosse D, Pagano S, Pagnacco E, Pierron F (2008) Overview of identification methods of mechanical parameters based on full-field measurements. Experimental Mechanics 48(4):381–402

[43] Grédiac M, Hild F (eds) (2012) Full-Field Measurements and Identification in Solid Mechanics. ISTE / Wiley, London (UK)

[44] Pierron F, Grédiac M (2021) Towards Material Testing 2.0. A review of test design foridentification of constitutive parameters from full-field measurements. Strain 57:e12370, 10.1111/str.12370

[45] Kavanagh KT, Clough RW (1971) Finite element applications in the characterization of elastic solids. Int J Solids Struct 7(1):11–23, 10.1016/0020-7683(71)90015-1

[46] Kavanagh KT (1972) Extension of classical experimental techniques for characterizing composite-material behavior. Exp Mech 12(1):50–56, 10.1007/BF02320791

[47] Pagnacco E, Caro-Bretelle A, Ienny P (2012) Parameter identification from mechanical field measurements using finite element model updating strategies. In: Grédiac M, Hild F (eds) Full-Field Measurements and Identification in Solid Mechanics, ISTE / Wiley, London (UK), pp 247–274

[48] Prates PA, Pereira AF, Sakharova NA, Oliveira MC, Fernandes JV (2016) Inverse Strategies for Identifying the Parameters of Constitutive Laws of Metal Sheets. Adv Mater Sci Eng 2016(Dic):1–18, 10.1155/2016/4152963

[49] Tarantola A (1987) Inverse Problems Theory. Methods for Data Fitting and Model Parameter Estimation. Elsevier Applied Science, Southampton (UK)

[50] Bertin M, Hild F, Roux S, Mathieu F, Leclerc H, Aimedieu P (2016) Integrated digital image correlation applied to elasto-plastic identification in a biaxial experiment. J Strain Anal Eng Des 51(2):118–131, 10.1177/0309324715614759

[51] Prates PA, Pereira AF, Oliveira MC, Fernandes JV (2019) Analytical sensitivity matrix for the inverse identification of hardening parameters of metal sheets. Eur J Mech A/Solids 75:205–215, 10.1016/j.euromechsol.2019.01.010

[52] Tomičević Z, Kodvanj J, Hild F (2016) Characterization of the nonlinear behavior of nodular graphite cast iron via inverse identification–Analysis of uniaxial tests. Eur J Mech A/Solids 59:140–154, 10.1016/j.euromechsol.2016.02.010

[53] Tomičević Z, Kodvanj J, Hild F (2016) Characterization of the nonlinear behavior of nodular graphite cast iron via inverse identification: Analysis of biaxial tests. Eur J Mech A/Solids 59:195–209, 10.1016/j.euromechsol.2016.03.006

[54] Réthoré J, Muhibullah ET, Coret M, Chaudet P, Combescure A (2013) Robust identification of elasto-plastic constitutive law parameters from digital images using 3D kinematics. Int J Solids Struct 50(1):73–85, 10.1016/j.ijsolstr.2012.09.002

[55] Wang Y, Coppieters S, Lava P, Debruyne D (2016) Anisotropic yield surface identification of sheet metal through stereo finite element model updating. J Strain Anal Eng Des 51(8):598–611, 10.1177/0309324716666437

[56] Lindner D, Mathieu F, Hild F, Allix O, Ha Minh C, Paulien-Camy O (2015) On the evaluation of stress triaxiality fields in a notched titanium alloy sample via integrated DIC. Journal of Applied Mechanics 82(7):071014

[57] Panwitt H, Heyer H, Sander M (2020) Experimental and Numerical Investigation of the Fracture Behavior of Welded Aluminum Cross Joints under Axial Compression. Materials 13(4310):1–23, 10.3390/ma13194310

[58] Brünig M, Zistl M, Gerke S (2021) Numerical Analysis of Experiments on Damage and Fracture Behavior of Differently Preloaded Aluminum Alloy Specimens. Metals 11(381):1–22, 10.3390/met11030381

[59] Pham CH, Adzima F, Coer J, Manach PY (2017) Anti-Buckling Device for Ultra-Thin Metallic Sheets Under Large and Reversed Shear Strain Paths. Exp Mech 57(4):593–602, 10.1007/s11340-017-0256-4

[60] Bertin M, Hild F, Roux S (2017) On the identifiability of the Hill-1948 model with one uniaxial tensile test. Comptes Rendus Mécanique 345(6):363–369, https://doi.org/10.1016/j.crme.2017.04.001

[61] Bertin M, Hild F, Roux S (2017) On the identifiability of Hill-1948 plasticity model with a single biaxial test on very thin sheet. Strain 53(5):e12233, https://doi.org/10.1111/str.12233

[62] Zhang P, Pereira M, Abeyrathna B, Rolfe B, Wilkosz D, Weiss M (2019) Improving the shear test to determine shear fracture limits for thin stainless steel sheet by shape optimisation. Int J Mech Sci 164:105116, 10.1016/j.ijmecsci.2019.105116

[63] Zaplatić A, Tomičević Z, Čakmak D, Hild F (2022) Improvement of the Arcan setup for the investigation of thin sheet behavior under shear loading. Exp Mech 62:313–332, 10.1007/s11340-021-00762-1

[64] Dufour J, Beaubier B, Roux S, Hild F (2014) Displacement measurement using CAD-based stereo-correlation with meshes. In: ICEM conference, 10.1007/978-3-319-06986-9_34

[65] Dubreuil L, Dufour JE, Quinsat Y, Hild F (2016) Mesh-based shape measurements with stereocorrelation. Exp Mech 56(7):1231–1242, 10.1007/s11340-016-0158-x

[66] Pierré JE, Passieux JC, Périé JN (2017) Finite Element Stereo Digital Image Correlation: Framework and Mechanical Regularization. Exp Mech 57(3):443–456, 10.1007/s11340-016-0246-y

[67] Dufour JE, Beaubier B, Hild F, Roux S (2015) CAD-based displacement measurements. Principle and first validations. Exp Mech 55(9):1657–1668, 10.1007/s11340-015-0065-6

[68] Yang DY, Kim JB, Yoon JW (2000) Wrinkling initiation and growth in modified Yoshida buckling test: Finite element analysis and experimental comparison. Int J Mech Sci 42:1683–1714, 10.1016/S0020-7403(99)00046-6

[69] Chen J, Yuan W, Wu W, Yang C (2020) Numerical simulation of wrinkling behavior for the tin plate. In: Procedia Manuf., vol 50, pp 429–432, 10.1016/j.promfg.2020.08.078

[70] Alimirzaei S, Mohammadimehr M, Tounsi A (2019) Nonlinear analysis of viscoelastic micro-composite beam with geometrical imperfection using FEM: MSGT electro-magneto-elastic bending, buckling and vibration solutions. Struct Eng Mech 71(5):485–502, 10.12989/sem.2019.71.5.485

[71] Pham DK, Pham CH, Hancock GJ (2022) Explicit approach for elastic local buckling analysis of thin-walled channels under combined bending and shear. Thin-Walled Struct 173:108925, 10.1016/j.tws.2022.108925

[72] Coulomb C (1821) Théorie des machines simples (in French). Bachelier, Paris (France)

[73] Armstrong PPJ, Frederick C (1966) A mathematical representation of the multiaxial bauschinger effect. CEGB Rep RD/B/N660 24:1–26

[74] Mathieu F, Leclerc H, Hild F, Roux S (2015) Estimation of elastoplastic parameters via weighted FEMU and integrated-DIC. Exp Mech 55(1):105–119, 10.1007/s11340-014-9888-9